

Particle-in-cell study of the ion-to-electron sheath transition

Brett Scheiner,^{1,a)} Scott D. Baalrud,¹ Matthew M. Hopkins,² Benjamin T. Yee,² and Edward V. Barnat²

¹Department of Physics and Astronomy, University of Iowa, Iowa City, Iowa 52240, USA

²Applied Optical and Plasma Sciences, Sandia National Laboratories, Albuquerque, New Mexico 87185, USA

(Received 28 April 2016; accepted 13 July 2016; published online 9 August 2016)

The form of a sheath near a small electrode, with bias changing from below to above the plasma potential, is studied using 2D particle-in-cell simulations. When the electrode is biased within $T_e/2e$ below the plasma potential, the electron velocity distribution functions (EVDFs) exhibit a loss-cone type truncation due to fast electrons overcoming the small potential difference between the electrode and plasma. No sheath is present in this regime, and the plasma remains quasineutral up to the electrode. The EVDF truncation leads to a presheath-like density and flow velocity gradients. Once the bias exceeds the plasma potential, an electron sheath is present. In this case, the truncation driven behavior persists, but is accompanied by a shift in the maximum value of the EVDF that is not present in the negative bias cases. The flow moment has significant contributions from both the flow shift of the EVDF maximum, and the loss-cone truncation. *Published by AIP Publishing.*

[<http://dx.doi.org/10.1063/1.4960382>]

I. INTRODUCTION

Electron sheaths can form around plasma boundaries that are biased above the plasma potential. In the absence of secondary emission of electrons from the boundary, the electrode can only be biased above the plasma potential in steady-state conditions provided that the electron collecting surface is small enough that global current balance in the plasma can be maintained.¹ This requirement that the electron collecting area is small typically precludes this situation from happening near large boundaries. Hence, electron sheaths are typically found around small electrodes.

The discussion of electron sheaths in the literature has traditionally assumed that such sheaths collect a random flux of electrons,^{2,3} do not pose a significant perturbation to the bulk plasma, and do not require any significant acceleration region for electrons entering the sheath.^{4,5} However, recent experiments and simulations at low temperature plasma conditions,⁶ along with theoretical work,⁷ have shown that the electron sheath is accompanied by a presheath-like region that accelerates electrons toward the electrode. In this presheath, the electrons achieve a flow moment comparable to the electron thermal speed by the sheath edge. Unlike the ion presheath, which accelerates ions through a ballistic response to the electric field, the electron presheath accelerates electrons through a force due to a pressure gradient. Simulations of the electron presheath have demonstrated that this pressure gradient term in the electron momentum equation is in fact the dominant term.⁷

The electron sheath and presheath are fundamental features of plasma boundary interactions. Although they have been rarely studied, there are potentially important applications of a deeper understanding of this fundamental phenomenon. One example is the low potential side of double layers, such as those found in the auroral upward current region⁸

and double layers in helicon plasma thrusters.⁹ Other areas where electron sheaths are known to be present are Langmuir probes collecting the electron saturation current,² tethered space probes,¹⁰ near electrodes used to induce circulation in dusty plasmas,¹¹ as well as the sheath prior to the formation of anode spots on small and gridded electrodes.^{12–14}

In this paper, the pressure-gradient-driven flow that arises as the bias of a small electrode is swept from several volts below to several volts above the plasma potential is studied using 2D particle-in-cell (PIC) simulations. During the transition from ion to electron sheath the electron velocity distribution function (EVDF) develops a loss cone as the electrode bias nears the plasma potential, an effect which has not been previously observed. As the electrode bias begins to exceed the plasma potential, the EVDF acquires a significant flow shift in addition to the loss cone. The nature of the EVDF in this transition is quantified by focusing on five electrode biases.

In case (A), the electrode is biased several times $T_e/2e$ below the plasma potential so that an ion sheath is present. Here, $T_e/2e$ is the typical change in potential seen in ion presheaths and is used as a measure of how weak the electrode can be biased below the plasma potential before a significant number of electrons overcome the potential barrier and are collected. In this case, nearly all electrons are repelled and the EVDF remains Maxwellian. Case (B) consists of an electrode biased less than $T_e/2e$ below the plasma potential. In this case the plasma remains quasineutral up to the electrode surface. At this bias, not all electrons are repelled resulting in the formation of a loss cone, which leads to presheath-like density and flow velocity gradients that increase as the electrode is approached. In case (C), when the electrode is biased nearly at the plasma potential, the loss cone and presheath-like gradients persist. In case (D), an electron sheath is observed at biases more than $T_i/2e$ but less than $T_e/2e$ above the plasma potential. Here, $T_i/2e$ is significant since below

^{a)}brett-scheiner@uiowa.edu

this bias a significant number of ions overcome the potential barrier and are collected by the electrode. In case (D), the EVDF continues to have a loss cone, but also has developed a significant flow shift. In case (E), the electrode is biased to a value much greater than the plasma potential. In this case the flow shift is more visible and the EVDF undergoes a distortion due to the acceleration in the strong electric field.

This paper is organized as follows. Sec. II describes the simulation setup and presents the key observations from simulations at different values of the electrode bias. Sec. III discusses the results of the simulations and explains the observations. Sec. IV gives concluding remarks.

II. SIMULATIONS

Simulations were performed using Aleph, an electrostatic PIC code.¹⁵ A 2D triangular mesh was used to discretize the 2D domain shown in Fig. 1(a). The 15 cm by 5 cm domain had three boundaries with a Dirichlet $V = 0$ boundary condition and one Neumann $\partial V/\partial y = 0$ boundary condition. The $V = 0$ boundaries were absorbing for particles, while the $\partial V/\partial y = 0$ boundary was reflecting. The Neumann condition with the reflecting boundary condition for particles represents an axis of symmetry for the system so that the simulation represents a physical area of 15 cm by 10 cm. An electrode of length 0.1 cm and width 0.02 cm was placed perpendicular to the center of the reflecting boundary. The time step of 50 ps resolved the electron plasma frequency and ensured that the plasma particles satisfied the Courant-Friedrichs-Lewy condition.¹⁶ Each simulation ran for 800000 time steps totaling 40 μ s of physical time. The duration of the simulation was long enough to ensure that a steady density, which occurred after approximately 35 μ s. The size of each mesh element was 0.02 cm, which resolved the electron Debye length. Particles included helium ions and electrons, each with a

macroparticle weight of 2000. The helium plasma was sourced in the volume at a rate of $10^8 \text{ cm}^{-3} \mu\text{s}^{-1}$ at temperatures of 0.08 eV for ions and 4 eV for electrons. The physical systems of interest are in a low pressure regime where the collisional mean free path for elastic electron scattering is much longer than the simulation domain, so interactions with neutral atoms were excluded.

Simulations for the five cases (A)–(E), mentioned previously in Sec. I, were carried out and results are summarized in Table I. The flow moments, densities for electrons and ions, and potential profiles are shown in Fig. 2. The figure displays values along a line perpendicular to the electrode, along the reflecting boundary. Here, the x axis is the distance from the center of the electrode along the line $y = 0$ in Fig. 1(a). These values are from the average of the last 100000 time steps of field data output by Aleph. Note that the non-smooth behavior in the velocity moment data is due to the velocity moment being a cell-based value, which is constant across each cell in the final output of the simulations. Since the simulations were 2D, the temperature values used here were computed from the x and y velocity components only, i.e., $T_e = n_e \int d^2 v m_e (v_{r,x}^2 + v_{r,y}^2) f_e / 2$, where f_e is the EVDF, n_e is the electron density, and $v_{r,i} = (\mathbf{v} - \mathbf{V}_e) \cdot \hat{\mathbf{i}}$. Two-dimensional velocity moments have previously been used when comparing theory to 2D simulations.^{7,17} The electron and ion flow velocities in Fig. 2 are normalized by $v_{T_e} = \sqrt{T_e/m_e}$ and $v_B = \sqrt{T_e/m_i}$, respectively. Here, the 2D values of T_e were computed approximately 0.5 cm from the electrode surface, and were 0.62 eV, 1.55 eV, 1.88 eV, 2.29 eV, and 5.17 eV for cases (A)–(E), respectively.

Using data from simulations the terms of the momentum equation

$$m_e n_e \mathbf{V}_e \cdot \nabla \mathbf{V}_e = -n_e \mathbf{E} - \nabla \cdot \mathcal{P}_e - \mathbf{R}_e \quad (1)$$

were evaluated. Here m_e , n_e , and \mathbf{V}_e are the electron mass, density, and flow moment, \mathcal{P}_e is the pressure tensor defined below, and \mathbf{R}_e is a friction term. The \hat{x} vector components $m_e n_e \mathbf{V}_e \cdot \nabla \mathbf{V}_e \cdot \hat{x}$ and $\nabla \cdot \mathcal{P}_e \cdot \hat{x}$ of the terms of the momentum equation were computed from particle location and velocity data at 20 different time slices separated by $5 \times 10^{-3} \mu\text{s}$ each. The velocity moments of the electron velocity distribution function $f_e(\mathbf{v})$ used above are

$$\mathbf{V}_e = \frac{1}{n_e} \int d^2 v v f_e(\mathbf{v}), \quad (2)$$

$$n_e = \int d^2 v f_e(\mathbf{v}), \quad (3)$$

and

TABLE I. Summary of the electrode bias ϕ_E , plasma potential ϕ_p , electron temperature T_e , and the desired value for $\phi_E - \phi_p$ in each simulation.

Simulation	ϕ_p (V)	ϕ_E (V)	T_e (eV)	Desired criteria for $\phi_E - \phi_p$
A	2.2	-25	0.62	$\phi_E - \phi_p < -T_e/2e$
B	5.7	5.5	1.55	$0 > \phi_E - \phi_p > -T_e/2e$
C	6.5	6.5	1.88	$\phi_E - \phi_p \sim 0$
D	7.6	8	2.29	$T_e/2e > \phi_E - \phi_p > T_i/2e$
E	18.5	25	5.17	$\phi_E - \phi_p > T_e/2e$

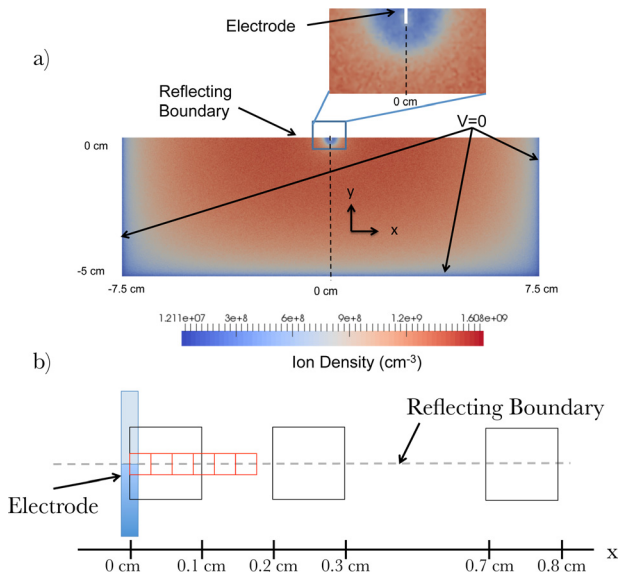


FIG. 1. (a) The simulation domain with a color map indicating the ion density. The electrode is placed perpendicular to the upper reflecting boundary and position along the horizontal axis is indicated by the dashed line. (b) Boxes displaying the limiting areas used for the calculation of EVDFs. The large black boxes were used for Fig. 3, while the small red boxes were used for Fig. 4.

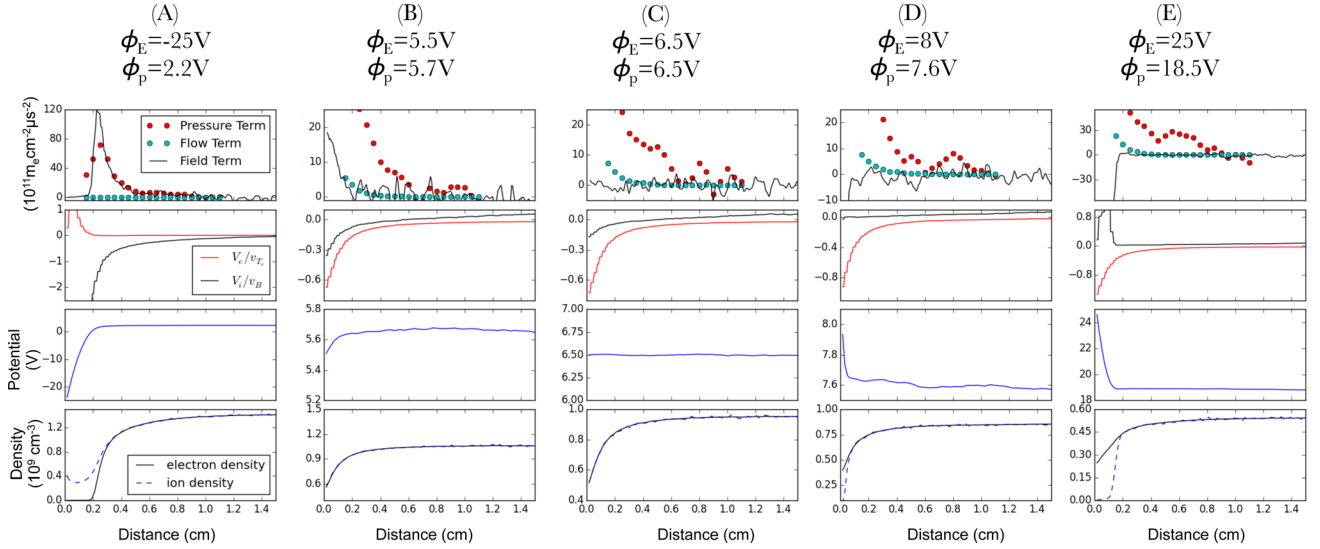


FIG. 2. Computed terms of the momentum equation, flow moments, potential, and density profiles for simulations (A)–(E). The data is plotted along the line $y = 0$, which runs perpendicular to the electrode surface, see Fig. 1(a). All quantities were calculated from mesh based values except for the pressure and flow terms of the momentum equation which were computed from particle positions and velocities as described in the text. In the top panel of each plot field term refers to $-ne\mathbf{E} \cdot \hat{x}$, flow term refers to $m_e n_e \mathbf{V}_e \cdot \nabla \mathbf{V}_e \cdot \hat{x}$, and the pressure term is $\nabla \cdot \mathcal{P}_e \cdot \hat{x}$. Note that the non-smooth behavior in the velocity moment data is due to this being a cell based quantity, which is output as constant across each cell.

$$\mathcal{P}_e = m_e \int d^2v (\mathbf{v} - \mathbf{V}_e)(\mathbf{v} - \mathbf{V}_e) f_e(\mathbf{v}) = p_e \mathcal{I} + \Pi_e, \quad (4)$$

where the pressure tensor is decomposed into the scalar pressure p_e multiplied by the identity tensor \mathcal{I} and stress tensor Π_e . Based on observation, it was assumed that the dominant gradients in \mathbf{V}_e and \mathcal{P}_e were in the \hat{x} direction. These moments along with the value of $-ne\mathbf{E} \cdot \hat{x}$ from the time averaged mesh based data are also shown in Fig. 2. All values were computed in 2D using only x and y velocity information.

Using particle location and velocity data from the same 20 time slices mentioned above, the EVDFs were obtained by plotting the 2D histogram of the x and y velocity components for particles. First, the distributions were obtained in three 0.1 by 0.1 cm boxes for all five simulations, the locations of which are indicated by the black boxes in Fig. 1(b). EVDFs for all simulations are shown in Fig. 3. For the case of the electrode biased at 25 V additional EVDFs, shown in Fig. 4, were obtained in the region indicated by the small red boxes in Fig. 1(b) to better resolve the EVDF within the sheath. A symmetric EVDF sampling region covers areas on both sides of the symmetry axis represented by the reflecting boundary, shown in Fig. 1(b). However, the domain only covers areas below this boundary. Particle velocity information above the reflecting boundary was obtained by reflecting the y velocity component of the particles in the lower half of the sampling region about the symmetry axis. For example, consider the black averaging boxes in Fig. 1(b). Here, only half of the desired sampling region is contained in the simulation domain since only one half of a 15 cm by 10 cm symmetric domain was simulated. The EVDF contribution from the other half of the sampling region was obtained by copying the particles contained in the 0.1 cm by 0.05 cm area below the symmetry axis, reflecting the y velocity component, and adding these particles to the original particles. The

interpretation of the data for these five simulations is discussed in Sec. III.

III. DISCUSSION

In Sec. II, simulations with five different values of electrode bias were presented: strong ion and electron sheath cases (A) and (E), and three cases (B)–(D) with the electrode biased near the plasma potential. In this section, flow moments and EVDFs calculated from these simulations are used to study the development of electron flow in the transition from ion to electron sheath.

First, the behavior of electrons near the strong ion sheath case (A) is examined. The fluid moments and fields for this case are shown in Fig. 2 and the EVDFs in Fig. 3. In the ion presheath and sheath, the electrons have no flow, except for a slight flow shift directed out of the sheath within 0.2 cm of the electrode. This is due to the expulsion of a small number of electrons sourced in the sheath. Although the flow is non-zero within 0.2 cm, the density is small enough that $n_e \mathbf{V}_e$ is negligible. The EVDFs show no truncation or flow shift, which corresponds to the expectation based on a Boltzmann density profile $n_e \sim \exp(-e\Delta\phi/T_e)$ in the presheath. This expectation is verified in Fig. 5 using the computed 2D electron temperature and simulated values of $\Delta\phi$. The EVDFs demonstrate that as the electrode is approached the density drops off rapidly, with only a few particles present within 0.1 cm of the electrode surface. A Boltzmann density profile is expected when the EVDF is Maxwellian, which can be seen from the electron momentum equation given in Eq. (1). In this case, friction and flow terms can be neglected, the pressure tensor reduces to $n_e T_e \mathcal{I}$, and its gradient is balanced by the electric field, leading to the exponential relation mentioned above. While other distributions might satisfy the zero flow moment requirement, the Maxwellian supports an

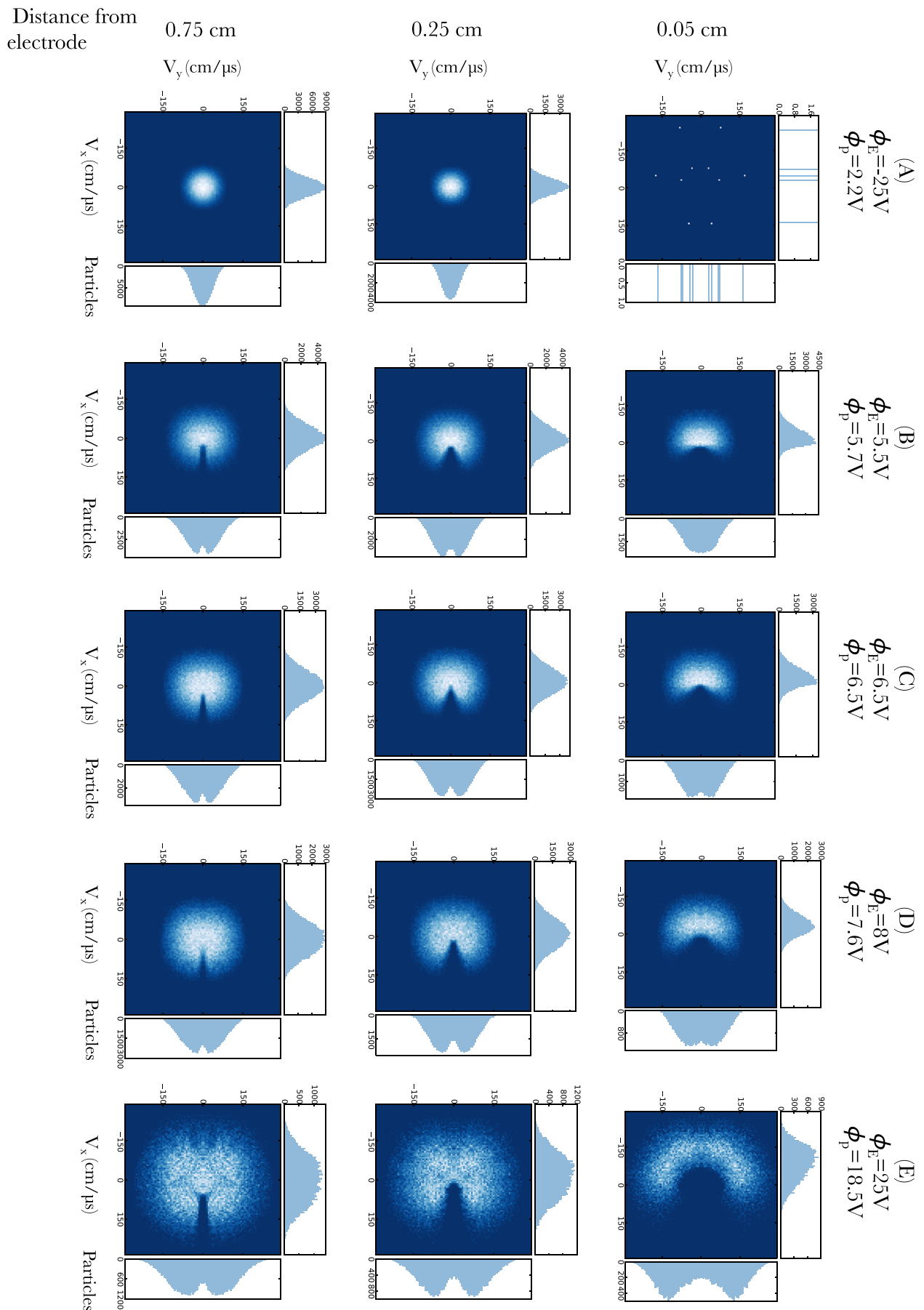


FIG. 3. EVDVs for simulations (A)–(E). The EVDF locations are marked as the centers of the black boxes shown in Fig. 1(b). The EVDF on the top left is next to the electrode and few electrons are present.

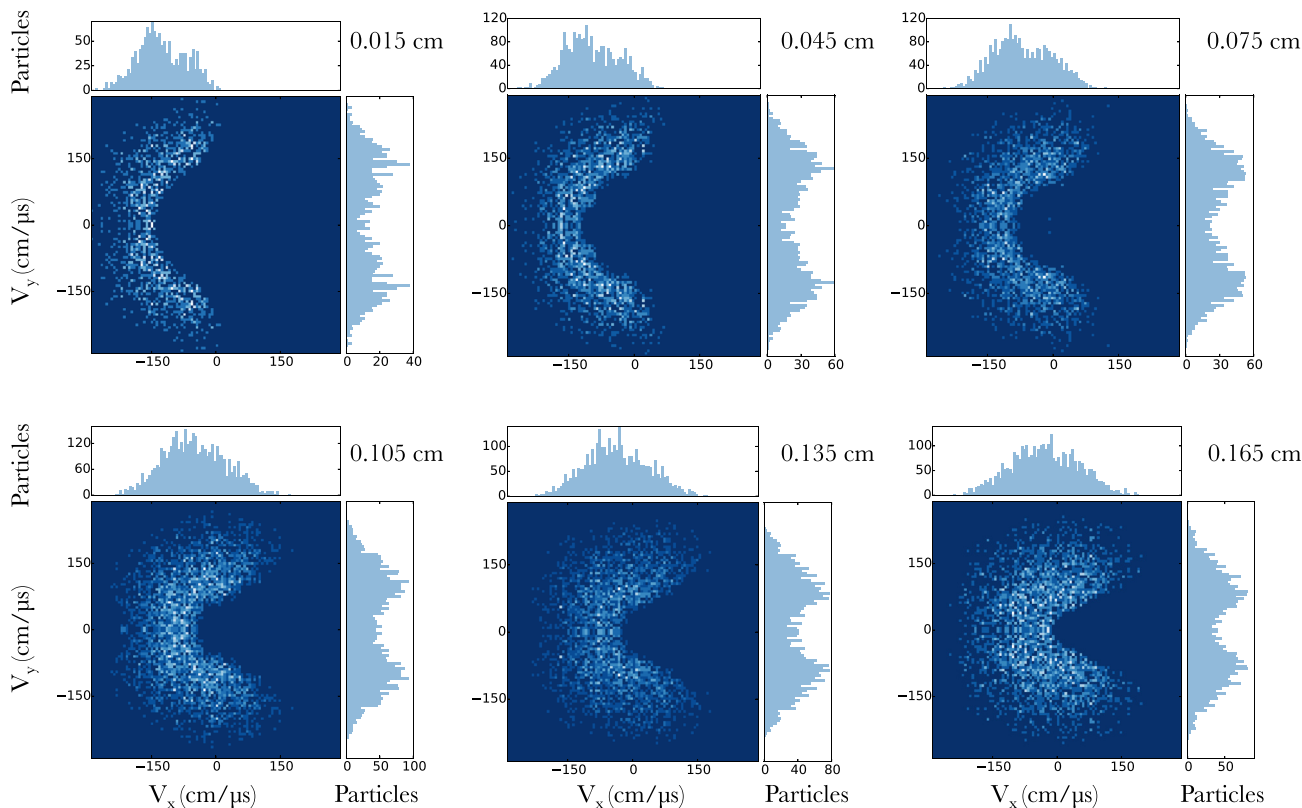


FIG. 4. EVDFs for simulation (E), the case of a strong electron sheath. The EVDF locations are marked as the centers of the red boxes shown in Fig. 1(b). Finer spatial resolution plots are shown to demonstrate the deformation of the EVDF within the electron sheath.

exponential decay for particles that follow characteristics defined by the electric field.¹⁸

In case (B), the electrode was biased within $T_e/2e$ below the plasma potential. Here the assumptions of the Boltzmann relation for the density profile break down. At such a small bias a significant number of electrons have energy greater than $T_e/2$ and reach the electrode, resulting in a truncation of the EVDF. The only electrons directed away from the electrode near its surface are those sourced in this region. However, this population is small and essentially negligible. The effects of this truncation can be seen in Fig. 3. Near the surface of the electrode, the truncated part of the EVDF forms a loss-cone type distribution with an angle that narrows when moving further into the bulk plasma. As shown in

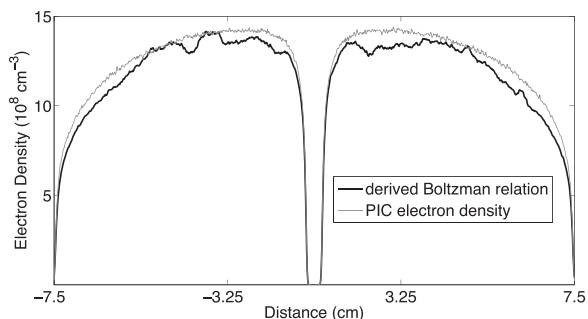


FIG. 5. Comparison of the electron density from simulation (A) with the Boltzmann relation using simulated values of the potential and the 2D temperature. The data is plotted along the line $y = 0$ in Fig. 1(a).

Fig. 6, there is an area that is geometrically inaccessible to electrons moving from left to right, forming a shadow. In this region, fast electrons directed towards the electrode are collected, and no electrons at high energy are available to fill in the part of the distribution directed away from the electrode. In the case of a strong ion sheath this does not occur, electrons directed towards the electrode are reflected and the distribution remains Maxwellian.

In the cases (B) and (C), the difference between the plasma potential and electrode are $0 > \phi_E - \phi_p > -T_e/2e$ and $\phi_E - \phi_p \sim 0$, as can be seen in the potential plotted in Fig. 2. The density profiles for ions and electrons, along with the small potential gradients, indicate that in these cases the plasma remains quasineutral up to the electrode. Although there is no breakdown of quasineutrality, there are still significant flow moments and density gradients for electrons

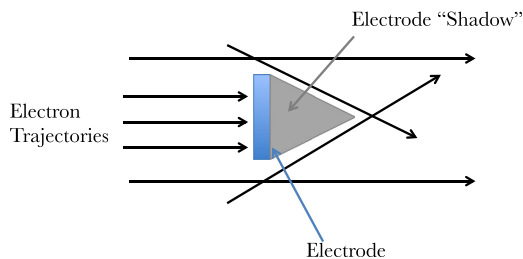


FIG. 6. Electron trajectories for right moving electrons are shown to demonstrate how a boundary can cause a truncation in a velocity distribution function, such as the loss-cone-like truncation.

and ions. Unlike the typical ion presheath, the ions only achieve a flow velocity of $\sim 0.4v_B$ by the electrode for case (B), while the electrons have a flow of $\sim 0.6v_{Te}$, with both flows directed towards the electrode. The electric field term for case (B) is weaker than the pressure term, and for case (C) the field term is negligible, suggesting the flows in this regime are not related to the electric field. Gradients in the electron densities and flow velocities can be explained by the widening of the loss cone. As the electrode is approached the loss cone angle increases while there is little or no shift in velocity of the maximum value of the EVDF in Fig. 3. The increasing flow moment is a result of the increasing angle of the loss cone. The continuity equation $\nabla \cdot (n_e \mathbf{V}_e) = 0$ requires that an increase in flow moment must be accompanied by a decrease in density. The computed velocity moment gradients in Fig. 2 indicate that the pressure tensor gradient, due to the increasing truncation, plays an important role when the electrode is biased near the plasma potential.

In case (D), the electrode was biased above the plasma potential. Here, qualitative changes in the EVDF and sheath structure were observed. The most notable difference is that the plasma no longer remains quasineutral up to the electrode, but a well defined electron sheath has formed. When $\phi_E - \phi_p \sim T_e/2e$ nearly all of the ions are repelled due to the fact that $T_e \gg T_i$. This can be seen in the ion density profile, which shows very few ions in the electron sheath. Here, the electrons achieve a flow velocity of $\sim 0.6\sqrt{T_e/m_e}$ by the sheath edge, which is slightly slower than the previously predicted value of $\sqrt{T_e/m_e}$.⁷ However, the exact sheath edge position is difficult to determine in time averaged data due to streaming instability driven fluctuations which have been discussed previously.⁷ Nevertheless, the flow of electrons into the sheath can be seen to be driven by pressure tensor gradients in Fig. 2, with some portion of the flow due to the shift in the maximum value of the EVDF, and the rest due to the truncation visible in Fig. 3.

The presheath behavior remains qualitatively similar as the electrode bias is further increased, as demonstrated by case (E). The presheath behavior is largely the same as that in case (D), a shift in maximum value of the EVDF and a loss cone is present near the sheath as shown in Fig. 3. The main difference between simulation (E) and simulation (D) is the deformation of the EVDF within the sheath, which is shown in detail in Fig. 4. Near the sheath edge, at $x = 0.165$ cm, the EVDF resembles the loss cone shaped distributions of Fig. 3. Moving into the sheath, the EVDF becomes stretched out, with electrode-directed electrons becoming more and more depleted due to the increasing strength of the electric field. A similar deformation of the EVDF has been seen in Vlasov simulations within the electron sheath around a cylindrical probe.¹⁹

The electron presheath behavior in simulations (D) and (E) were slightly different than that previously described in the 1D model of Ref. 7; however, it also shares some of the same qualities. Previous analysis was based on the 1D projections of the EVDF which look largely Maxwellian in the direction perpendicular to the electrode surface. Based on the observation of 1D EVDFs the electron presheath was modeled describing the electrons with a flow-shifted

Maxwellian and ions with a Boltzmann density profile. Using these assumptions, the dominant term in the electron momentum equation, Eq. (1), is the pressure gradient, which was T_e/T_i larger than contribution of the presheath electric field. This model proposed a significant deviation from the conventional assumption of a half-Maxwellian at the sheath edge.^{3,20,21} It also showed that the electron sheath has a presheath that causes a significant perturbation far into the plasma. The results in this paper present a refined picture compared to the previous 1D model. Like the 1D model, a long presheath was visible in the electron flow moments shown for simulations (D) and (E) in Fig. 2. The EVDFs discussed above demonstrate that, for the electron sheath cases, the flow velocity is due to both a loss-cone like truncation and a flow shift. The truncation due to the loss cone leads to a significant contribution to the acceleration of the flow moment through pressure tensor gradients in the momentum equation. The pressure driven behavior was previously explained using only a scalar pressure gradient in the 1D model of Ref. 7, and did not include the physics of the loss-cone truncation. Finally, the loss-cone truncation was found to be a geometric effect related to electron collection by the electrode, which originates in case (B) in which they are no longer strongly repelled.

IV. CONCLUSION

In this paper, the physics of the sheath and presheath was explored using electron velocity data from 2D PIC simulations. When the electrode was biased within $T_e/2e$ below the plasma potential, the plasma remained quasineutral up to the electrode surface, but still had presheath-like density and flow velocity gradients for both electrons and ions. Using EVDFs obtained from individual electron velocity data, the flow and density gradients were shown to originate from a loss-cone-like truncation of the EVDF due to fast electrons overcoming the $\sim T_e/2e$ potential barrier. This was described as an effect of the breakdown of the assumptions behind the Boltzmann density relation, which arises due to a gradient in the stress tensor.

When an electron sheath was present, the EVDFs had flow velocity moments with contributions from both a flow shift, and a loss-cone-like truncation. As the electrode was approached from the bulk plasma, the loss cone angle was observed to widen, increasing the flow moment and was accompanied by a flow-shift driven by a pressure tensor gradient. The onset of the loss-cone behavior was observed to arise when the electrode bias is sufficiently close to the plasma potential that electrons were not completely repelled, leading to an addition to the pressure tensor gradient term in Eq. (1). This contribution was due to the increasing value of the stress tensor, in Eq. (4), which grows in magnitude as the electrode is approached and the EVDF truncation becomes more pronounced.

ACKNOWLEDGMENTS

The first author would like to thank James Franek and Andrew Fierro for reading the manuscript. This research was supported by the Office of Fusion Energy Science at the U.S.

Department of Energy under Contract No. DE-AC04-94SL85000. The first author was also supported by the U.S. Department of Energy, Office of Science, Office of Workforce Development for Teachers and Scientists, Office of Science Graduate Student Research (SCGSR) program. The SCGSR program was administered by the Oak Ridge Institute for Science and Education for the DOE under Contract No. DE-AC05-06OR23100.

- ¹S. D. Baalrud, N. Hershkowitz, and B. Longmier, *Phys. Plasmas* **14**, 042109 (2007).
- ²H. M. Mott-Smith and I. Langmuir, *Phys. Rev.* **28**, 727 (1926).
- ³N. Hershkowitz, *Phys. Plasmas* **12**, 055502 (2005).
- ⁴K.-U. Riemann, *J. Phys. D: Appl. Phys.* **24**, 493 (1991).
- ⁵F. F. Chen, *Plasma Sources Sci. Technol.* **15**, 773 (2006).
- ⁶B. T. Yee, B. Scheiner, S. D. Baalrud, E. V. Barnat, and M. M. Hopkins, e-print [arXiv:1508.05971](https://arxiv.org/abs/1508.05971) [physics.plasm-ph].
- ⁷B. Scheiner, S. D. Baalrud, B. T. Yee, M. M. Hopkins, and E. V. Barnat, *Phys. Plasmas* **22**, 123520 (2015); e-print [arXiv:1510.03490](https://arxiv.org/abs/1510.03490) [physics.plasm-ph].
- ⁸R. E. Ergun, L. Andersson, D. Main, Y.-J. Su, D. L. Newman, M. V. Goldman, C. W. Carlson, A. J. Hull, J. P. McFadden, and F. S. Mozer, *J. Geophys. Res.* **109**, A12220, doi:10.1029/2004JA010545 (2004).
- ⁹C. Charles and R. W. Boswell, *Appl. Phys. Lett.* **91**, 201505 (2007).
- ¹⁰N. Singh and A. Jaggernauth, *J. Geophys. Res.* **101**, 17229, doi:10.1029/96JA00925 (1996).
- ¹¹D. A. Law, W. H. Steel, B. M. Annaratone, and J. E. Allen, *Phys. Rev. Lett.* **80**, 4189 (1998).
- ¹²B. Song, N. D'Angelo, and R. L. Merlino, *J. Phys. D: Appl. Phys.* **24**, 1789 (1991).
- ¹³S. D. Baalrud, B. Longmier, and N. Hershkowitz, *Plasma Sources Sci. Technol.* **18**, 035002 (2009).
- ¹⁴R. L. Stenzel, C. Ionita, and R. Schrittwieser, *Plasma Sources Sci. Technol.* **17**, 035006 (2008).
- ¹⁵H. Timko, P. S. Crozier, M. M. Hopkins, K. Matyash, and R. Schneider, *Contrib. Plasma Phys.* **52**, 295 (2012).
- ¹⁶R. Courant, K. Friedrichs, and H. Lewy, *Math. Annal.* **100**, 32 (1928).
- ¹⁷S. D. Baalrud, B. Scheiner, B. Yee, M. Hopkins, and E. Barnat, *Plasma Phys. Controlled Fusion* **57**, 044003 (2015); e-print [arXiv:1412.4826](https://arxiv.org/abs/1412.4826) [physics.plasm-ph].
- ¹⁸J. Clerk-Maxwell, *Nature* **8**, 537 (1873).
- ¹⁹G. Sánchez-Arriaga, *Phys. Plasmas* **20**, 013504 (2013).
- ²⁰G. Medicus, *J. Appl. Phys.* **32**, 2512 (1961).
- ²¹G. Medicus, *J. Appl. Phys.* **33**, 3094 (1962).